# Identification of corrosion damage in submerged structures using fundamental anti-symmetric Lamb waves

**Jiangang Chen, Zhongqing Su[1] and Li Cheng**

Department of Mechanical Engineering, The Hong Kong Polytechnic University, Kowloon,
Hong Kong SAR

E-mail: MMSU@polyu.edu.hk

## Abstract

Corrosion is a representative modality of damage in metallic structures serving in humid or corrosive environments, and examples include petroleum pipelines immersed underwater or buried underground. To facilitate awareness of corrosion at its initial stage is a key measure to prevent further deterioration and failure of these structures. A damage identification approach capitalizing on the fundamental anti-symmetric Lamb wave mode ($A_0$) and in terms of a pulse-echo measurement scheme was developed for evaluating corrosion in submerged structures. However the presence of a coupled fluid medium and changes in its properties exert influence on the propagation characteristics of the $A_0$ mode in the structures at a phenomenal level, leading to erroneous identification without appropriate rectification. Allowing for this, the effect arising from fluid coupling on the $A_0$ mode was investigated and calibrated quantitatively, whereby rectification and compensation were applied to the identification. The proposed approach was numerically and experimentally validated by evaluating through-thickness hole and chemical corrosion in submerged aluminium plates, with the assistance of a probability-based diagnostic imaging approach. Identification results have demonstrated the necessity of rectification and compensation for the medium coupling effect when applying Lamb-wave-based damage identification to structures with coupled media.

(Some figures in this article are in colour only in the electronic version)

## 1. Introduction

Corrosion, the disintegration of material into its constituent atoms as a result of chemical or electro-chemical reactions with the surroundings [1], is a typical damage modality in a wide range of metallic engineering structures and in particular aircraft components, petroleum pipelines, offshore platform and boat/submarine hulls. Working in humid or corrosive environments, these structures are prone to corrosion in the presence of moisture or fluid. Corrosion gives rise to reduction in material thickness due to loss of atoms from the surface [2], consequently causing fragility, impairing integrity and shortening service lifetime of the structures. Such a concern is particularly accentuated for transportation vehicles and petro-chemical pipelines whose failure as a result of poor integrity potentially leads to catastrophic consequences.

With the attempt to identify damage including corrosion in metallic structures at an early stage so as to prevent further failure occurring, nondestructive evaluation (NDE) techniques have been entailed over the years, exemplified by magnetic particle inspection [3, 4], magnetic flux leakage technique [5, 6], pressure testing [7], shearography, magnetic resonance imagery, laser interferometry, acoustic holography, infrared thermography, acoustic emission, radiography and eddy currents [3, 4]. In spite of success in a number of applications, these NDE techniques have been increasingly challenged on their practicability and convenience when applied to real engineering structures in service. Most of the approaches request termination of normal service of the structures to be inspected and removal of the insulation layers

---

[1] Author to whom any correspondence should be addressed.

if any, incurring high cost in terms of labour and disruption to the service; some may become inefficient when applied to nonferrous materials, magnetic-mechanism-based approaches in particular; and as a result of negligence of influence from moisture/fluid, identification errors are often produced.

Lamb waves, the form of guided elastic waves in thin plate/shell-like structures, have been intensively examined as a promising candidate to develop cost-effective NDE in the past two decades [8–12], because of their superb capabilities, including low attenuation even when propagating in structures underwater, strong penetration, fast propagation, omnidirectional dissemination, convenience of activation and acquisition, inexpensive implementation, low energy consumption and, most importantly, high sensitivity to structural damage and material inhomogeneities even when they are small in size or lie beneath the surface. Featuring these merits Lamb waves have great potential to be used for detecting damage in submerged structures. Representatively, for inspecting defects in underwater pipes, Na and Kundu [7] developed a coupler mechanism and designed an innovative transducer holder to activate anti-symmetric (flexural) cylindrical Lamb waves at various incident angles and frequencies. Mijarez *et al* [13] used piezoelectric transducers, permanently attached to the inner wall of hollow sub-sea members of offshore steel oilrigs and powered by a normally inert seawater battery, to generate and collect cylindrical Lamb waves. Both studies proposed different mode selection criteria for picking up the most appropriate wave modes for identification of defects. In this aspect, the effect of fluid coupling on Lamb wave propagation was often not concerned.

In this study, a Lamb-wave-based identification approach was developed for evaluating damage and corrosion in particular in submerged structures, by taking advantage of the fundamental anti-symmetric mode, $A_0$. In a relatively low frequency range (up to 1 MHz · plate thickness), such a wave mode features a smaller wavelength compared with its symmetric counterparts widely employed in previous studies [9, 10, 12], therefore able to pinpoint damage of a smaller dimension. However anti-symmetric Lamb wave modes are much more sensitive to the presence of surrounding media and changes in their properties than symmetric modes [14, 15], posing a challenge in delivering correct identification without appropriate rectification. As a prerequisite of implementing Lamb-wave-based identification to submerged structures, the influence arising from the coupled fluid medium on Lamb wave propagation in solid structures was investigated and then calibrated quantitatively. The rectified approach by considering medium coupling was numerically and experimentally validated by evaluating a through-thickness hole, as a feasibility study, and chemical corrosion, as an application, in submerged aluminium plates, with the assistance of a probability-based diagnostic imaging technique.

## 2. Lamb waves in submerged solids

Lamb waves are elastic disturbances in thin plates or shells (with planar dimensions being far greater than that of the

thickness and with the wavelength being in the order of the thickness) that provide upper and lower boundaries to guide continuous propagation of the waves.

### 2.1. Lamb waves in free solid medium

Lamb waves, comprised of longitudinal and transverse waves, manifest themselves as the superposition of symmetric and anti-symmetric modes, which can be described by [16],

$$\frac{\tan(qh)}{\tan(ph)} = -\frac{4k^2qp}{(k^2-q^2)^2} \qquad \text{for symmetric modes,} \quad (1a)$$

$$\frac{\tan(qh)}{\tan(ph)} = -\frac{(k^2-q^2)^2}{4k^2qp} \qquad \text{for anti-symmetric modes}$$
$$(1b)$$

where

$$p^2 = \frac{\omega^2}{c_L^2} - k^2, \qquad q^2 = \frac{\omega^2}{c_T^2} - k^2, \qquad k = \frac{2\pi}{\lambda_{\text{wave}}},$$

$$c_L = \sqrt{\frac{2\mu(1-\nu)}{\rho(1-2\nu)}}, \qquad \text{and} \qquad c_T = \sqrt{\frac{\mu}{\rho}}.$$

$h$, $k$, $\omega$ and $\lambda_{\text{wave}}$ are half plate thickness, wavenumber, circular frequency and wavelength of the Lamb waves, respectively. $c_L$ and $c_T$ are the velocities of longitudinal and transverse waves, respectively ($\rho$, $\mu$ and $\nu$ are the density, shear modulus and Poisson's ratio of the medium, respectively). Symbols $S_i$ and $A_i$ ($i = 0, 1, \ldots$) in what follows stand for the symmetric and anti-symmetric wave modes, respectively, with the subscript being the order. In particular $S_0$ and $A_0$ are the fundamental symmetric and anti-symmetric modes, respectively.

As with most guided waves, Lamb waves are dispersive, and their velocities are dependent on both the wave frequency and plate thickness, as seen in the dispersion curves of Lamb waves in an aluminium plate shown in figure 1 [17]. At any frequency, the $S_0$ and $A_0$ modes co-exist and higher-order modes appear as frequency increases. Less-dispersive regions exist in the low frequency range where fundamental modes travel at almost constant velocities, referred to as the *non-dispersion region*, as highlighted in figure 1 for the $S_0$ and $A_0$ modes. With constant propagation velocities, the $S_0$ and $A_0$ modes in the non-dispersion region are widely employed to develop damage identification techniques.

### 2.2. Lamb waves in fluid–solid coupled medium

Extending the above discussion to the media consisting of distinct components coupled together, such as a plate immersed in liquid or buried in soil. With confinement to the plate surfaces, a surrounding medium such as fluid provides a radiation way for Lamb waves to leak outwards from the solids. When leaky waves meet the boundary of the coupled medium, they will be reflected back to the solids, disseminating throughout the coupled medium. This coupling effect may modulate the propagation characteristics of Lamb waves in the solids significantly. For different Lamb modes, such an influence can be distinct. In essence, when a plate is submerged in fluid, $S_i$ modes will mostly be retained in the plate since
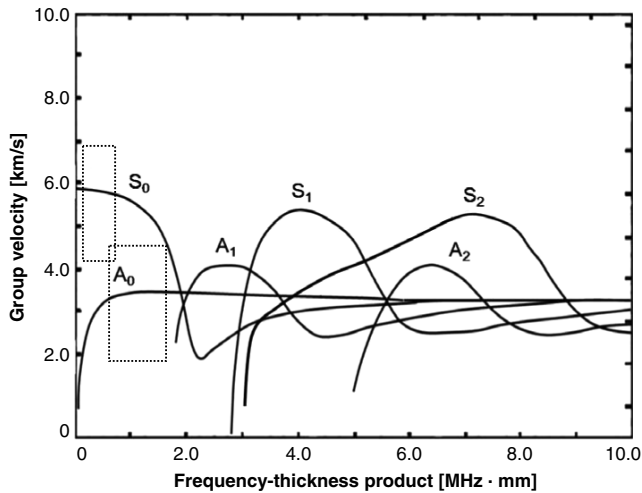
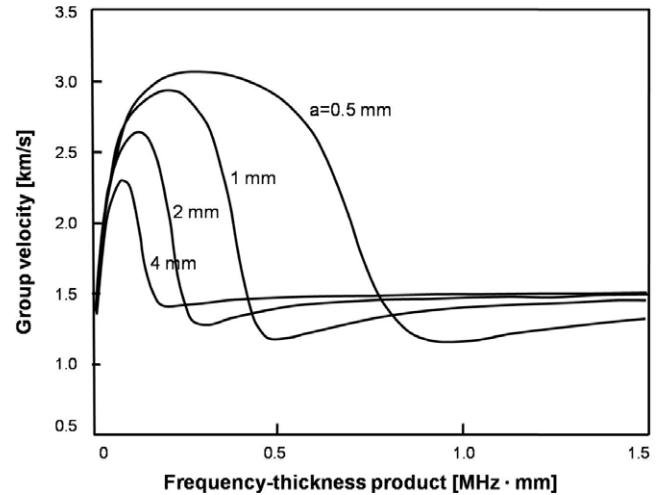**Figure 1.** Dispersion curves of Lamb waves in a free aluminium plate [17] (dotted area: less-dispersion region).



**Figure 2.** Dispersion curves of Lamb waves (showing the $A_0$ mode only) in an aluminium plate coupled with a water layer (*a*: thickness of the water layer) [18].

it is difficult for the in-plane particle motion to cross the plate–liquid interface ($S_i$ modes predominantly have radial in-plane displacement of particles), and as a result there is no pronounced energy leakage from the plate to the surrounding medium for the $S_i$ modes. However, partial energy of the $A_i$ modes will leak into the fluid ($A_i$ modes mostly have out-of-plane displacement). The leaky Lamb waves behave differently from Lamb waves in free solids.

If both the solid and fluid media are deemed isotropic in nature whereas the latter is unable to sustain shear loads, the characteristic equation for an infinitely large fluid–solid coupled medium, with the fluid layer thickness being *a* and plate thickness being *b*, can be described as [18]

$$\det(G(\omega, k, c_F, c_L, c_T, a, b, \rho_F, \rho)) = 0, \qquad (2)$$

where $\rho$ and $\rho_F$ are the densities of the solid substrate and coupled fluid medium; $c_F$ is the bulk velocity of waves in the fluid. $G$ is the characteristic matrix for the coupled medium [18]. Solutions to equation (2) are the dispersion curves of Lamb waves in a coupled medium, as displayed in figure 2 for the $A_0$ mode in an aluminium plate coupled with a water layer as an example [18]. Comparing figures 1 and 2, a prominent discrepancy for the $A_0$ mode propagating in the free solid and fluid-coupled solid can be observed.

*2.3. Lamb-wave-based damage identification*

Lamb waves have been the core of intensive efforts for developing cost-effective damage identification over the past two decades. In the majority of studies [9, 10, 12], the $S_0$ mode is selected for damage identification, due to, in contrast to the $A_0$ mode, its:

 (i) lower attenuation (the $A_0$ mode usually presents higher attenuation during propagation because of the dominant out-of-plane movement of particles in the mode, which leaks partial energy to the surrounding medium; whereas the $S_0$ mode has mostly in-plane displacement and thereby its energy is confined within the plate);

 (ii) faster propagation velocity, meaning that complex wave reflection from the structural boundary can be avoided in some cases; and

(iii) lower dispersion, facilitating signal interpretation.

On the other hand, there has been increasing awareness of using the $A_0$ mode for damage identification [19–21]. The merits of this mode, in comparison with the $S_0$ mode, include:

 (i) shorter wavelength at a given excitation frequency and therefore higher sensitivity to damage of small size, in recognition of the fact that the half wavelength of a selected mode must be shorter than or equal to the damage size to allow the wave to interact with damage;

 (ii) larger signal magnitude (the $A_0$ mode in a Lamb wave signal is usually much stronger than the $S_0$ mode at relatively low frequencies (e.g., 150 kHz used in this study), giving a signal with high signal-to-noise ratio, though as mentioned earlier it attenuates more quickly); and

(iii) easier means of activation (the out-of-plane motion of particles in a plate can more easily be activated using ultrasonic transducers that can generate out-of-plane vibration including piezoelectric elements used in the current study).

Generally speaking, both the $S_0$ and $A_0$ modes can be used for identifying a variety of structural damage, although the $S_0$ mode exhibits higher sensitivity to damage in the structural thickness and delamination in particular [22–24], whereas the $A_0$ mode outperforms the $S_0$ mode with higher sensitivity to surface damage such as cracks, corrosion [25] or surface crack growth [26]. In recognition of the above observations and in particular the fact that the $A_0$ mode features a smaller wavelength in the relatively low frequency range compared with its symmetric counterparts and therefore enables scrutiny of damage of smaller dimension, the $A_0$ mode was employed for corrosion identification in this study.
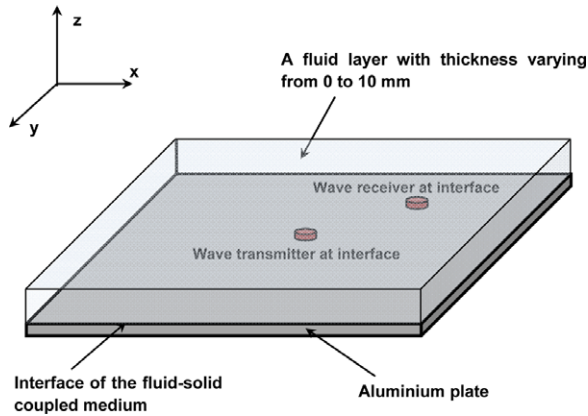
**Figure 3.** Schematic of transmitter and receiver allocation for examining Lamb wave propagation in the fluid–solid coupled medium (distance between the transmitter and sensor: 175 mm).

**Table 1.** Material properties of aluminium and fluid for FE simulation and experimental validation.

|           | Density (kg m$^{-3}$) | Young's modulus (GPa) | Poisson's ratio | Bulk modulus (GPa) |
|-----------|------------|------------|------------|------------|
| Aluminium | 2711       | 71         | 0.35       |            |
| Fluid     | 1000       |            |            | 2.2        |

## 3. Investigation of fluid coupling effect on Lamb wave propagation

Nevertheless as aforementioned, the $A_0$ mode behaves differently in a submerged solid from the way it does in a free solid as a consequence of the medium coupling effect [14, 15, 18]. A quantitative calibration of such influence was conducted numerically and experimentally for developing the $A_0$ mode-based corrosion identification.

### 3.1. Finite element (FE) simulation

Considering a square aluminium plate measuring 600 mm × 600 mm × 1.6 mm and supported on its four edges, the upper surface of the plate was in contact with a fluid layer of the same planar area whose thickness varied from 0 to 10 mm with an increment of 0.5 mm, as shown schematically in figure 3. Material properties of the selected aluminium and fluid are summarized in table 1. The aluminium plate and fluid layer were simulated using three-dimensional eight-node brick solid elements and three-dimensional eight-node acoustic elements, respectively. To ensure simulation accuracy, the largest dimension of FE elements was less than 1 mm, guaranteeing that at least ten elements were allocated per wavelength of the $A_0$ mode (wavelength of the $A_0$ mode at the frequency of 150 kHz is circa 15 mm). In the acoustic elements, acoustic pressure was applied in the $z$-axis only, see figure 3 for the coordinate system, in conformity to the fact that fluid is unable to withstand shear loads within the $x$–$y$ plane.

The interface between the fluid layer and aluminium plate was simulated using a surface-based coupling constraint provided by ABAQUS®/EXPLICIT in terms of a node-to-surface formulation, called '*TIE*'. Such a constraint allows
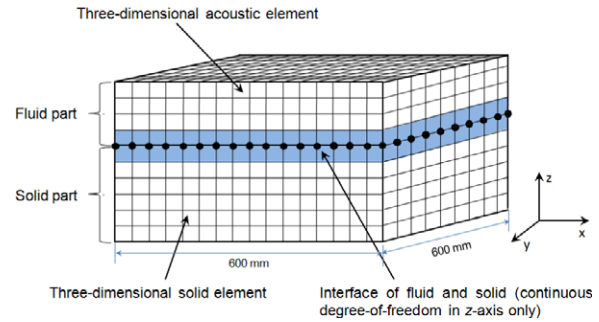


**Figure 4.** Schematic of '*TIE*' constraint for simulating the interface of fluid–solid coupled medium.

a mixture of rigid and deformable portions of a surface, as elucidated schematically in figure 4. The coupling constraints force the degrees-of-freedom in the $z$-axis equal for a pair of surfaces, of which one is designated to be the master surface (solid surface) and the other be the slave surface (fluid surface). Simulated by '*TIE*', motions of particles at the interface are continuous in the out-of-plane direction ($z$-axis), but not in $x$–$y$ plane, the same as in reality.

To generate Lamb waves in the fluid–solid coupled medium, a pre-developed piezoelectric transmitter model [27] was employed and positioned at the planar centre of the interface, as shown in figure 3. Uniform vertical ($z$-axis) displacements were applied on FE nodes of the transmitter model, to generate the $A_0$ mode dominating the signal energy, in recognition of the fact that $A_i$ modes mostly have out-of-plane displacement. With the transmitter model, five-cycle *Hanning* window-modulated sinusoid tonebursts at a central frequency of 150 kHz were activated [27]. Such a frequency, in the non-dispersion region aforementioned, is lower than the cut-off frequencies of higher-order modes in the discussed aluminium plate, and as a consequence only the $S_0$ and $A_0$ modes co-exist. At this frequency, the $A_0$ mode features higher magnitude in a captured signal in comparison with the $S_0$ mode. Upon propagating in the coupled medium, Lamb wave signals at the interface were captured with a pre-developed piezoelectric receiver model [27], 175 mm apart from the transmitter. Dynamic FE simulation was accomplished using the commercial FE package ABAQUS®/EXPLICIT. The step of the calculation time was controlled to be less than the ratio of the minimum distance of any two adjoining nodes to the maximum velocity of involved wave mode, namely, the $S_0$ mode. The above modelling and simulation were repeated in the absence and presence of fluid layers of different thicknesses ranging from 0 to 10 mm with an increment of 0.5 mm. As an example, the FE model when the fluid layer was 4 mm in thickness is exhibited in figure 5.

### 3.2. Experimental validation

In parallel to FE simulation, experimental validation was conducted under room temperature in which all the material and geometric properties of the solid and fluid media, as well as setup configurations, remained the same as those in the FE simulation. A pair of water-proof immersion transducers
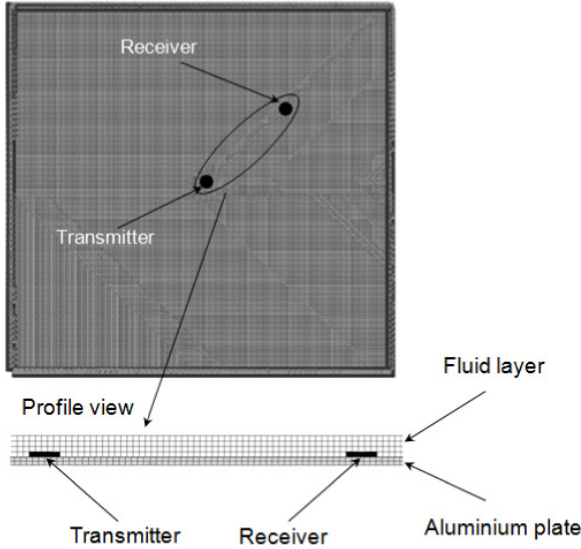
**Figure 5.** An FE model for the fluid–solid coupled medium (when the fluid layer is 4 mm in thickness) containing a piezoelectric wave transmitter and receiver.

(Panametrics-NDT™-V303-SU, central frequency: 1 MHz, diameter: 13 mm) were collocated in tandem at the fluid–solid interface, serving as the wave transmitter and receiver to generate and collect Lamb wave signals, respectively. The transmitter was positioned at the centre of the aluminium plate while the receiver was 175 mm apart from the transmitter, both of which were then instrumented with a signal generation/acquisition system developed on a *VXI* platform [27, 28], shown schematically in figure 6. A fluid layer with its thickness varying from 0 to 10 mm with an increment of 0.5 mm was introduced in contact with the upper surface of the aluminium plate, consistent with FE simulation. Five-cycle *Hanning* window-modulated sinusoid tonebursts at a central frequency of 150 kHz were generated with a signal generation unit (Agilent® E1441), amplified to 180 $V_{p-p}$ with a linear signal amplifier (Piezo Systems® EPA-104), and then applied to the transmitter. The Lamb wave signals were captured with a signal digitizer (Agilent® E1438A) at a sampling rate of 25 MHz.

### 3.3. Signal processing and results

As representative results, raw Lamb wave signals captured at the interface (including both the $S_0$ and $A_0$ modes) in the absence and presence of a fluid layer of 4 mm in thickness are compared in figure 7. To facilitate signal interpretation, all the numerically and experimentally obtained signals were applied with a Hilbert-transform-based signal processing technique [29–31]. Aimed at canvassing a dynamic signal in terms of its energy distribution, the Hilbert transform is defined as [8]

$$H(t) = \frac{1}{\pi} \int_{-\infty}^{+\infty} \frac{f(\tau)}{t - \tau} \, \mathrm{d}\tau. \qquad (3)$$

$H(t)$ is the Hilbert transform of signal $f(t)$. Equation (3) performs a 90° phase-shift or quadrature filter to construct a
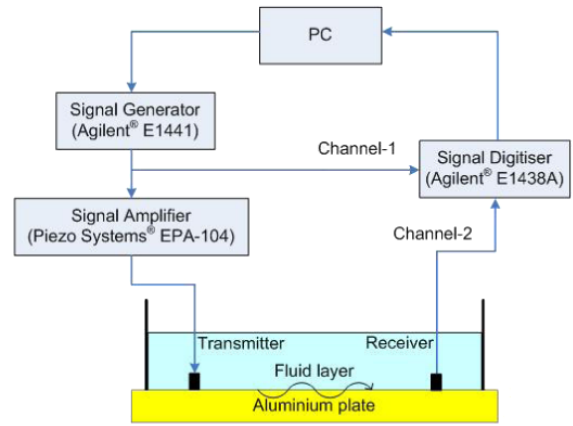


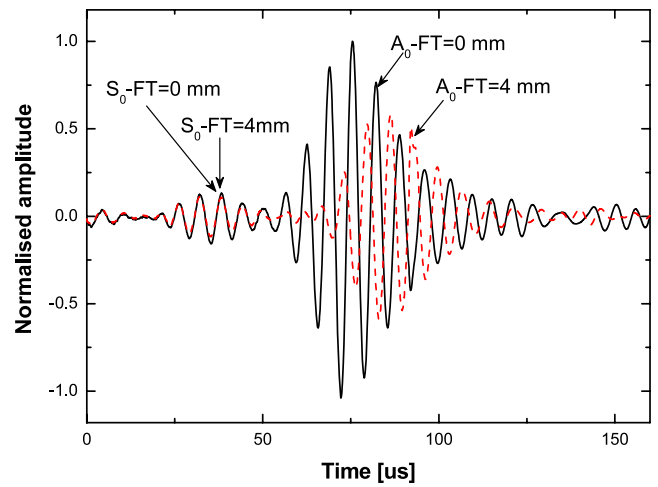**Figure 6.** Setup for experimental validation.



**Figure 7.** Captured raw Lamb wave signals at the interface in the absence and presence of a fluid layer of 4 mm in thickness (FT: fluid layer thickness).

so-called analytic signal $F_A(t)$:

$$F_A(t) = f(t) + \mathrm{i}H(t) = e(t)\mathrm{e}^{\mathrm{i}\phi(t)}, \qquad (4a)$$

$$e(t) = \sqrt{f^2(t) + H^2(t)}, \qquad \text{and}$$

$$\phi(t) = \frac{1}{2\pi} \frac{\mathrm{d}}{\mathrm{d}t} \arctan \frac{H(t)}{f(t)}, \qquad (4b)$$

where $e(t)$ is the module of $F_A(t)$ and its envelope depicts the energy distribution of $f(t)$ in the time domain. For illustration, the Hilbert-transform-processed results of signals shown in figure 7 are exhibited in figure 8. For comparison, figure 8 also includes the Hilbert-transform-processed signals when the thickness of the fluid layer was 1, 6 and 9 mm, respectively.

In figure 8, the first energy concentration is recognized as the $S_0$ mode which features the highest propagation velocity at the given frequency of 150 kHz; the second concentration is the $A_0$ mode which dominates the signal energy at the frequency of 150 kHz and therefore presents a greater magnitude than that of the $S_0$ mode. It can be observed that the fluid layer does not exert prominent influence on the $S_0$ mode, whereas
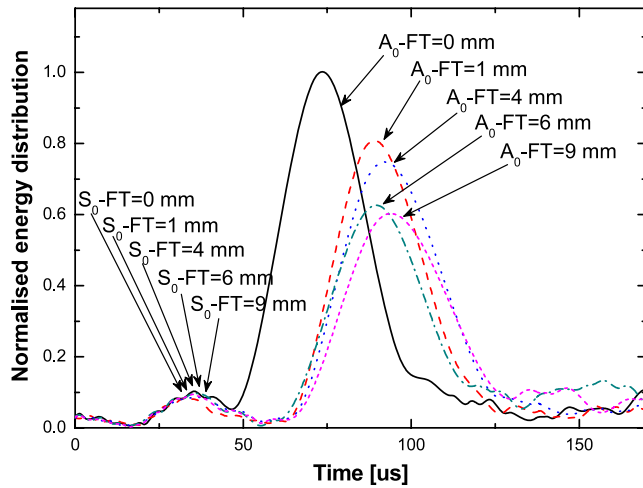
**Figure 8.** Hilbert-transform-processed wave signals at the interface in the absence and presence of fluid layers of different thicknesses (FT: fluid layer thickness).

the $A_0$ mode at a significant degree, manifesting as twofold: (i) reduction in the signal/energy magnitude; and (ii) delay in the arrival time as a result of reduced propagation velocity, as summarized in figure 9.

In particular, the most obvious changes in magnitude of signal energy and propagation velocity of the $A_0$ mode take place when the fluid layer is initially introduced, but such changes fluctuate slightly with a further increase of the thickness of the fluid layer. The slight fluctuation rather than monotonic decrease in the signal magnitude and velocity as fluid thickness increases can be attributed to the measurement errors and uncertainties. The above observation recapitulates that the out-of-plane movement of particles in the $A_0$ mode provides a radiation way for Lamb waves to leak outwards into the surrounding coupled medium. The fluid load, in turn, affects the wave propagation of the $A_0$ mode in the solids. This is however not the case for the $S_0$ mode which dominates the in-plane vibration mode. To facilitate understanding, figure 10 presents the energy distribution of a Lamb wave propagating in the fluid–solid coupled medium via FE simulation. In the diagram, partial energy of the $A_0$ mode can be seen to leak to the fluid layer from the plate, whereas no significant energy leakage to the fluid layer for the $S_0$ mode can be captured. It is the primary mechanism of greater signal attenuation of the anti-symmetric modes in a coupled medium when compared with the symmetric modes.

Extending the above examination by exciting Lamb waves in a sweep frequency range from 50 to 350 kHz, dispersion curves of the fundamental Lamb wave modes in the aluminium plate in the absence and presence of a fluid layer of 4 mm in thickness were achieved experimentally and numerically, as displayed in figure 11. Based on the above results, the influence of fluid coupling on the propagation of the $A_0$ mode in the solids was quantitatively calibrated, subject to the thickness of the fluid layer.
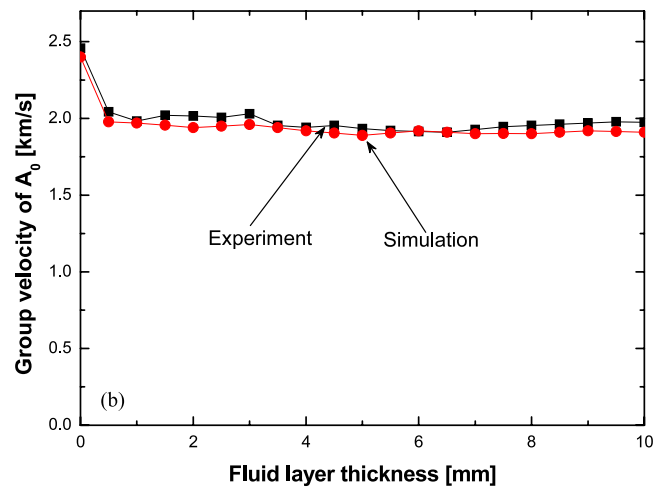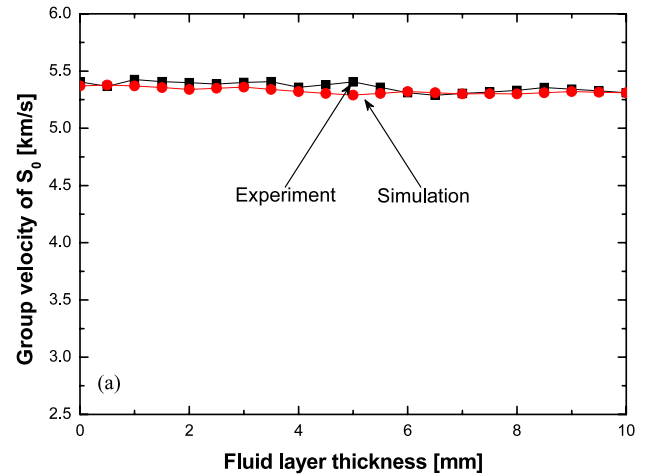


**Figure 9.** Group velocity of the (a) $S_0$ mode and (b) $A_0$ mode in the aluminium plate coupled with a fluid layer versus thickness of the fluid layer, obtained via FE simulation and experiment.

## 4. Probability-based diagnostic imaging using time-of-flight (ToF)

There has been increasing interest in presenting damage identification results intuitively in a two-dimensional image whose pixels correspond exclusively to spatial points of the structure under inspection, i.e., diagnostic imaging [28–30, 32–34]. Such an identification approach attempts to describe damage using a greyscale image in which the field values at pixels indicate the probability of damage presence; and the region shaped by pixels at which the field values are above a threshold may further be assumed to represent the damage size.

In the study, a probability-based diagnostic imaging approach was employed using ToF extracted from captured Lamb wave signals for establishing the probability at pixels [28]. ToF is herein defined as the time consumed for a wave to travel a certain distance [28]. Considering a transmitter–receiver pair (i.e., a sensing path; in what follows *transmitter* is denoted by subscript '$T$', *receiver* is denoted by subscript '$R$' and *damage* is denoted by subscript '$D$'),
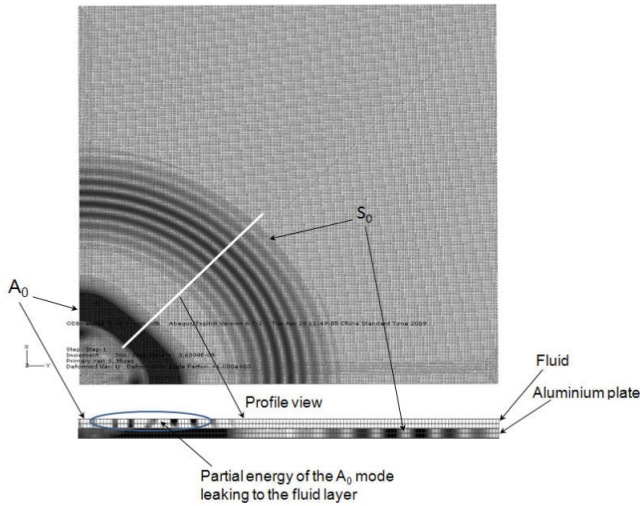
**Figure 10.** Stress distribution of Lamb wave propagating in a fluid–solid coupled medium, showing energy leakage of the $A_0$ mode (for comparison, displayed stress distribution in the fluid layer and in the aluminium plate is not of the same scale; the darker the greyscale the higher the stress is).

figure 12, it has,

$$t_{T-D-R} - t_{T-R} = \left( \frac{L_{T-D}}{V} + \frac{L_{D-R}}{V} \right) - \frac{L_{T-R}}{V} = \Delta t, \quad (5)$$

where

$$L_{T-D} = \sqrt{(x_D - x_T)^2 + (y_D - y_T)^2},$$

$$L_{D-R} = \sqrt{(x_D - x_R)^2 + (y_D - y_R)^2},$$

and

$$L_{T-R} = \sqrt{(x_T - x_R)^2 + (y_T - y_R)^2}.$$

In the above equation, $t_{T-D-R}$ is the ToF of the incident wave propagating from the transmitter to the damage and then to the receiver; $t_{T-R}$ is the ToF of the incident wave propagating directly from the transmitter to the receiver. $\Delta t$ is the difference between the above two ToFs, which can be ascertained from a captured wave signal. $L_{T-D}$ is the distance between the transmitter located at $(x_T, y_T)$ and the damage centre presumed at $(x_D, y_D)$ and to be determined; $L_{D-R}$ is the distance between the damage centre and the receiver located at $(x_R, y_R)$; $L_{T-R}$ is the distance between the transmitter and receiver. $V$ is the group velocity of the selected Lamb wave mode, namely, $A_0$ in this study, activated by the transmitter.

Theoretically, solutions to equation (5) configure a locus of the roots, the dotted ellipse in figure 13, indicating possible locations of the damage which reflect the perceptions as to damage in the structure from the perspective of the transmitter–receiver pair that creates such a locus. For a given transmitter–receiver pair, a greyscale image can be constructed in which the field value at a specific pixel is calibrated in terms of the shortest distance between this pixel and the locus established by the transmitter–receiver pair. This is driven by the hypothesis that the pixels right on the locus have the highest degree of probability (100%) as to the presence of damage,
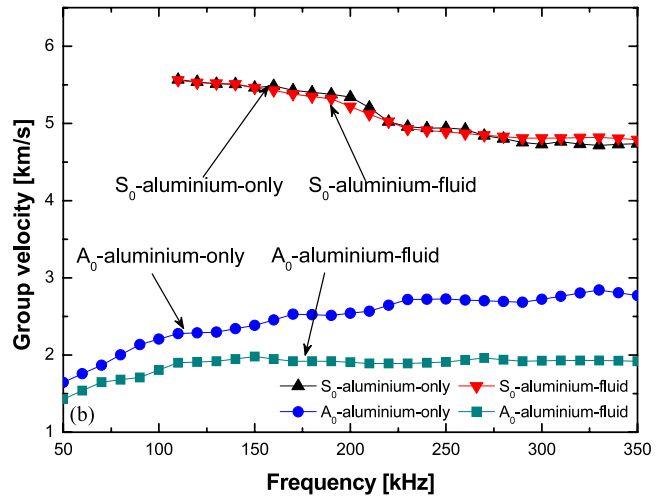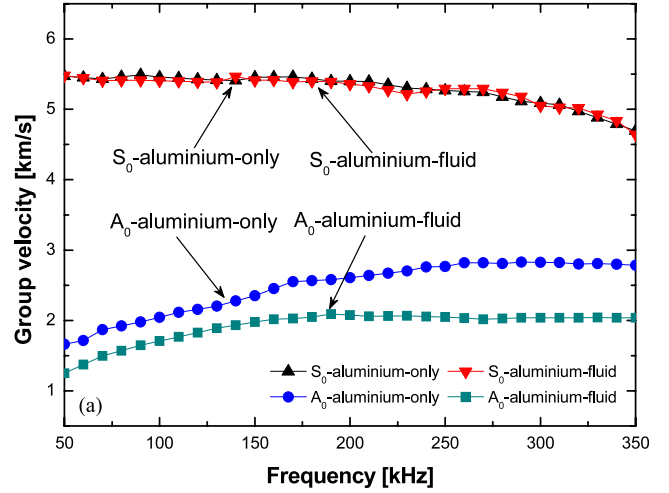


**Figure 11.** Dispersion curves of Lamb waves in an aluminium plate in the absence and presence of a fluid layer (4 mm in thickness) obtained via (a) FE simulation and (b) experiment.
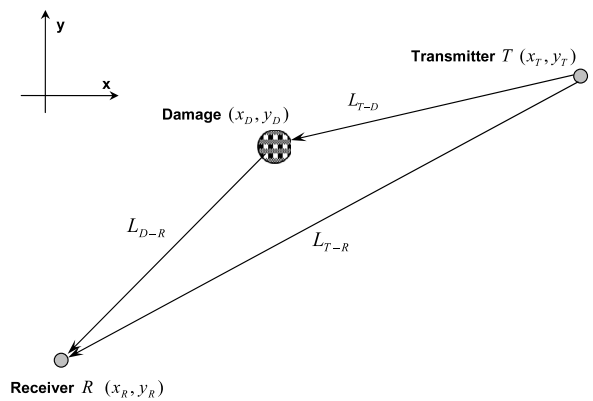


**Figure 12.** Relative positions among transmitter, receiver and damage for a sensing path.

and for other pixels, the greater the distance to the locus, the lower the probability that damage exists there. To establish probabilities at pixels in relation to the loci created by different transmitter–receiver pairs, a *cumulative distribution function*
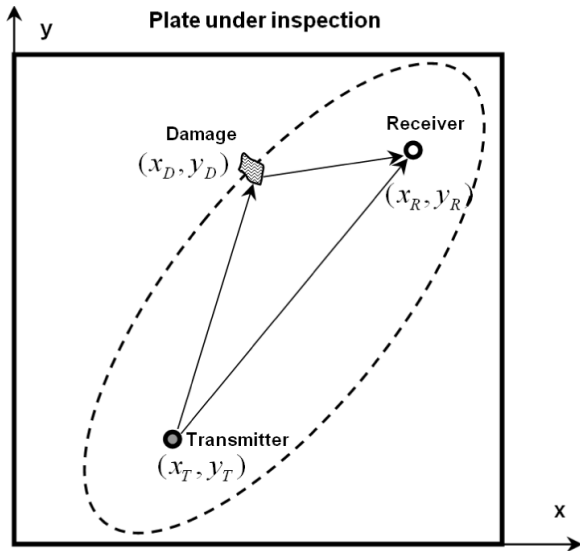
**Figure 13.** Locus of roots to equation (5) established by a sensing path, indicating possible locations of damage in the structure.

(CDF) [35], $F(z)$, was introduced, which is defined as

$$F(z) = \int_{-\infty}^{z} f(z_{ij}) \, \mathrm{d}z_{ij}, \tag{6}$$

where $f(z_{ij}) = \frac{1}{\sigma_{ij}\sqrt{2\pi}} \exp[-\frac{z_{ij}^2}{2\sigma_{ij}^2}]$ is the *Gaussian distribution function*, representing the probability density function (PDF) of damage at pixel $(x_m, y_m)$, $(m = 1, 2, \ldots, K$, for the structure under inspection whose corresponding greyscale image has $K$ pixels), perceived by the sensing path connecting the transmitter $T_i$ and receiver $R_j$ ($i = 1, 2, \ldots, N$, and $j = 1, 2, \ldots, M$ for the case that $N$ transmitters and $M$ receivers are considered). $z_{ij} = \sqrt{(x_m - x_{ij})^2 + (y_m - y_{ij})^2}$, where $(x_{ij}, y_{ij})$ is the location on the locus established by sensing path $T_i - R_j$ that has the shortest distance to pixel $(x_m, y_m)$. $\sigma_{ij}$ is the standard variance, describing the variability or dispersion of a data set, which was set as 0.44 in the present study. Given a distance, $z_{ij}$, the probability of the presence of damage at pixel $(x_m, y_m)$ established by sensing path $T_i - R_j$, $I(x_m, y_m)|_{ij}$ (i.e., the field value of the greyscale image at pixel $(x_m, y_m)$), is

$$I(x_m, y_m)|_{ij} = 1 - [F(z_{ij}) - F(-z_{ij})]. \tag{7}$$

Following the above steps, each sensing path contributes a greyscale image indicating the probability of the presence of damage at a specific pixel. Upon aggregation of such greyscale images contributed by all the available sensing paths via appropriate image fusion, damage in the structure, if any, can be highlighted at pixels where the field values (probabilities) are greater than a preset threshold. Details of the probability-based diagnostic imaging can be referred to elsewhere [28].

## 5. Feasibility study: identifying through-thickness hole in a submerged aluminium plate

For validation, the quantitatively calibrated influence of fluid coupling on Lamb wave propagation was applied to the
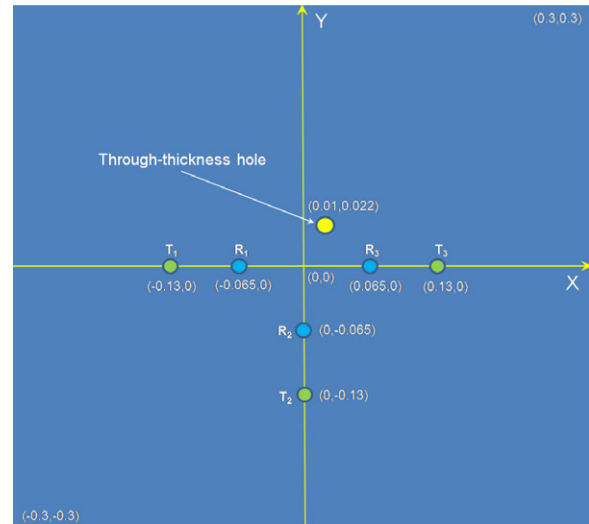


**Figure 14.** An aluminium plate containing a through-thickness hole for feasibility study of the approach (unit: m).

evaluation of a through-thickness hole (15 mm in diameter) in a submerged aluminium plate (600 mm × 600 mm × 1.6 mm) using the probability-based diagnostic imaging. The upper surface of the aluminium plate was in contact with a fluid layer of varying thickness. To prevent leakage of fluid through the hole, the hole was sealed with a thin film from the lower surface of the plate (opposite to the fluid layer). A pair of water-proof immersion transducers, the same as that described in section 3, was employed to perform a pulse-echo measurement at different positions at the interface of the fluid layer and aluminium plate, offering three sensing paths, $T_1 - R_1$, $T_2 - R_2$ and $T_3 - R_3$, as indicated in figure 14. Signal generation/acquisition was accomplished with the system developed on a *VXI* platform (figure 6). Five-cycle *Hanning*-windowed sinusoid tonebursts at a central frequency of 150 kHz were excited and applied to three transmitters in turn after amplified to $180V_{p-p}$. The Lamb wave signals were then captured via three sensing paths at a sampling rate of 25 MHz.

As demonstrated previously, propagation characteristics of the $A_0$ mode are significantly modulated when the fluid layer is initially introduced, but little affected with a further increase in thickness of the fluid layer. Allowing for this, only the fluid layers of 4 and 7 mm in thickness, respectively, were considered. Figure 15(a) shows the Hilbert-transform-processed signals experimentally captured via sensing path $T_3 - R_3$, as example, in the absence and presence of fluid layers of different thicknesses (4 and 7 mm, respectively). For comparison, signals via the same sensing paths obtained using the FE simulation technique introduced in section 3.1 is presented in figure 15(b). Upon ascertainment of the difference in ToFs between the incident and through-thickness hole-scattered $A_0$ mode, probabilities of damage presence at pixels can be calculated in terms of equation (7) for individual sensing paths, to create probability greyscale images. Representatively, the image established by $T_1 - R_1$ when the fluid thickness was 4 mm is displayed in figure 16. Furthermore, the aggregated greyscale images by fusing individual images contributed by
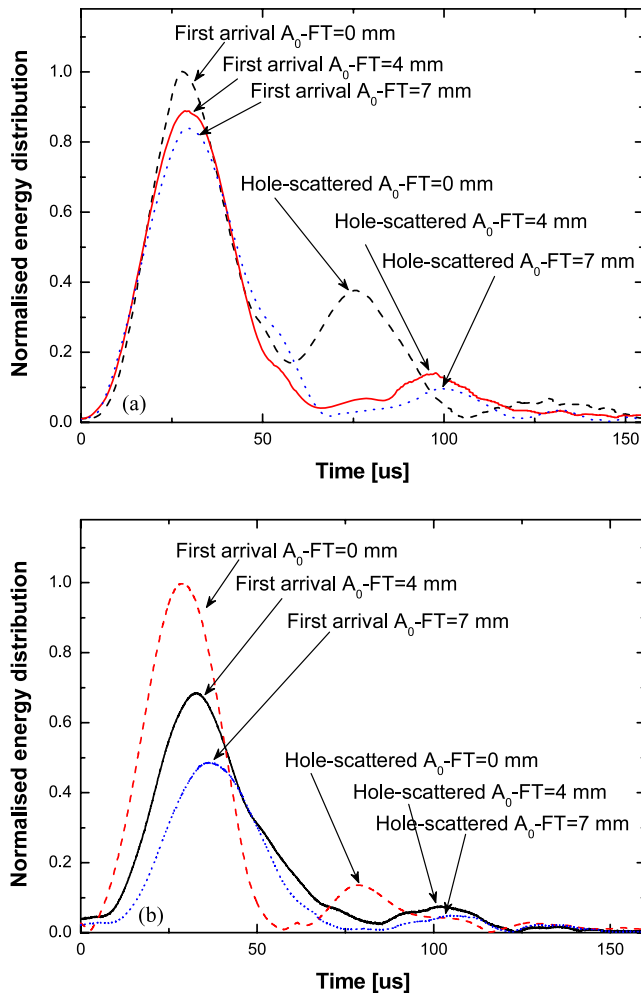
**Figure 16.** A probability greyscale image as to the damage established by sensing path $T_1 - R_1$ when the fluid layer is 4 mm in thickness (the darker the greyscale the higher the probability of damage presence is).

**Figure 15.** Hilbert-transform-processed wave signals captured via sensing path $T_3 - R_3$ in the aluminium plate containing a through-thickness hole in the absence and presence of fluid layers of different thicknesses, obtained via (a) experiment and (b) FE simulation (FT: fluid layer thickness).

three sensing paths are displayed in figure 17, for without and with the rectification and compensation for the fluid coupling influence on Lamb wave propagation. Using the wave propagation velocity as that in the absence of fluid and ignoring the fluid coupling effect, a large discrepancy between the identified results and real location of the through-thickness hole is observed in figures 17(a) and (b), irrespective of thickness of the fluid layer; in contrast, as observed in figures 17(c) and (d), using the rectified wave propagation velocity by compensating for the fluid coupling effect, the identified damage matches well with the actual damage (if 85% of the maximum of field values in the probability image was set as the threshold to draw an explicit conclusion that damage takes place), irrespective of thickness of the fluid layer.

## 6. Application: evaluating corrosion damage in a submerged aluminium plate

As application, the developed approach was employed to evaluate corrosion damage in a submerged aluminium plate.
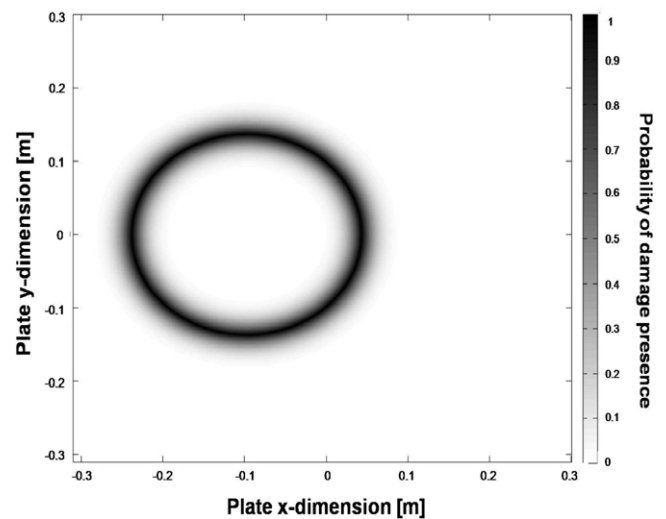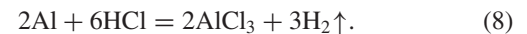
A chemical corrosion was pre-introduced to an aluminium plate (600 mm × 600 mm × 1.6 mm) by exposing a quasi-circular zone on the plate to 45% hydrochloric acid (Advanced Technology & Industrial Co., Ltd), in the light of

$$2Al + 6HCl = 2AlCl_3 + 3H_2\uparrow. \qquad (8)$$

The produced chemical substances were removed after the chemical reaction completed and the surface of the corroded area was polished with a sand paper. The above operation was repeated until a corroded area, measuring roughly 15 mm in diameter and 1 mm in depth, was formed, as shown in figure 18. Lamb wave signals were excited and captured via three sensing paths, $T_1 - R_1$, $T_2 - R_2$ and $T_3 - R_3$, respectively, with the same configurations used in the feasibility study.

Figure 19 shows the Hilbert-transform-processed signals experimentally captured via sensing path $T_3 - R_3$, as example, in the absence and presence of fluid layers of different thicknesses (4 and 7 mm, respectively). Similar to those observations in the feasibility study, the corrosion-scattered $A_0$ mode can clearly be identified in the Hilbert-transform-processed signals. Following the steps of probability-based diagnostic imaging, each sensing path contributed a probability image. Upon fusion of images, the identified results are shown in figure 20, for without and with the rectification and compensation for the fluid coupling influence on Lamb wave propagation. Using the rectified wave propagation velocity by compensating for the fluid coupling effect, it can be seen that the identification results of corrosion damage in the submerged aluminium plate are satisfactory whatever the thickness of the fluid layer is. For the sake of brevity, only the results obtained via experiment were presented in figure 20, although good agreement between FE simulation and experiment was achieved.

As observed in both the experiment and simulation, there is no phenomenal discrepancy in the degree of modulation
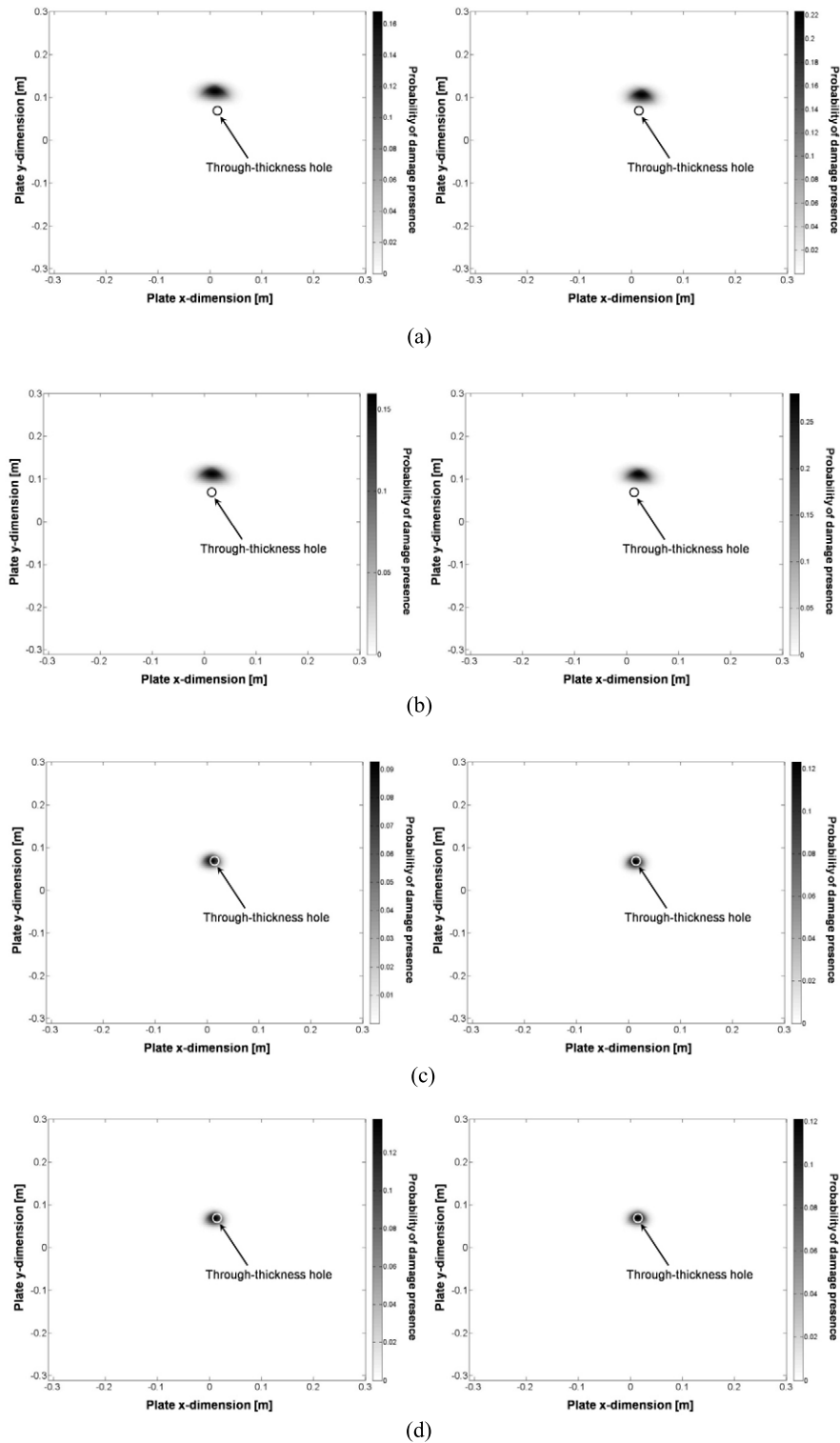
(a)



(b)



(c)



(d)

**Figure 17.** Identification results of a through-thickness hole in the aluminium plate coupled with fluid layers of different thicknesses: (a) without rectification (left: experiment result; right: simulation result) when the fluid layer is 4 mm in thickness; (b) without rectification (left: experiment result; right: simulation result) when the fluid layer is 7 mm in thickness; (c) with compensation for the coupling effect (left: experiment result; right: simulation result) when the fluid layer is 4 mm in thickness, and (d) with compensation for the coupling effect (left: experiment result; right: simulation result) when the fluid layer is 7 mm in thickness (white or black circle: actual damage).

on the $A_0$ mode from fluid coupling when the fluid layer has different thicknesses, whereas the most prominent modulation takes place when the fluid layer is initially introduced, implying that the surrounding fluid medium exerts significant influence on Lamb wave propagation only in a confined area. This makes it possible to apply the compensation
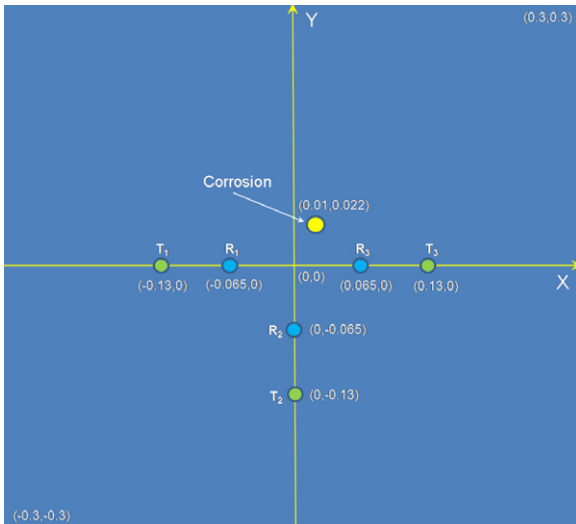
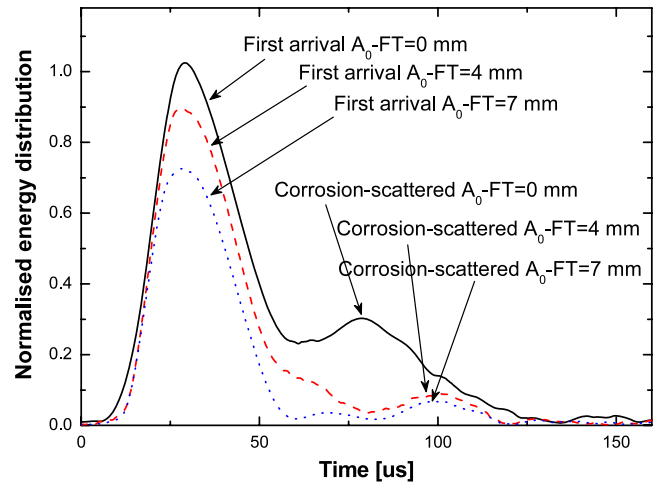**Figure 18.** An aluminium plate containing corrosion damage (unit: m).



**Figure 19.** Hilbert-transform-processed wave signals captured via sensing path $T_3 - R_3$ in the aluminium plate containing corrosion damage in the absence and presence of fluid layers of different thicknesses, obtained via experiment (FT: fluid layer thickness).

for the coupling effect on Lamb wave propagation at a specific thickness of the fluid layer to the submerged structures regardless of difference in thickness of the coupled fluid media.

## 7. Conclusion

The $A_0$ mode was adopted to identify corrosion damage in submerged metallic structures by taking advantage of its short wavelength and therefore high sensitivity to damage of small dimension. However, the surrounding fluid medium modulates the propagation characteristics of the $A_0$ mode in the structures phenomenally, leading to erroneous identification without appropriate rectification. The effect arising from the coupled fluid medium on the $A_0$ mode was investigated and calibrated quantitatively. Based on appropriate compensation for the coupling effect, structural damage including a
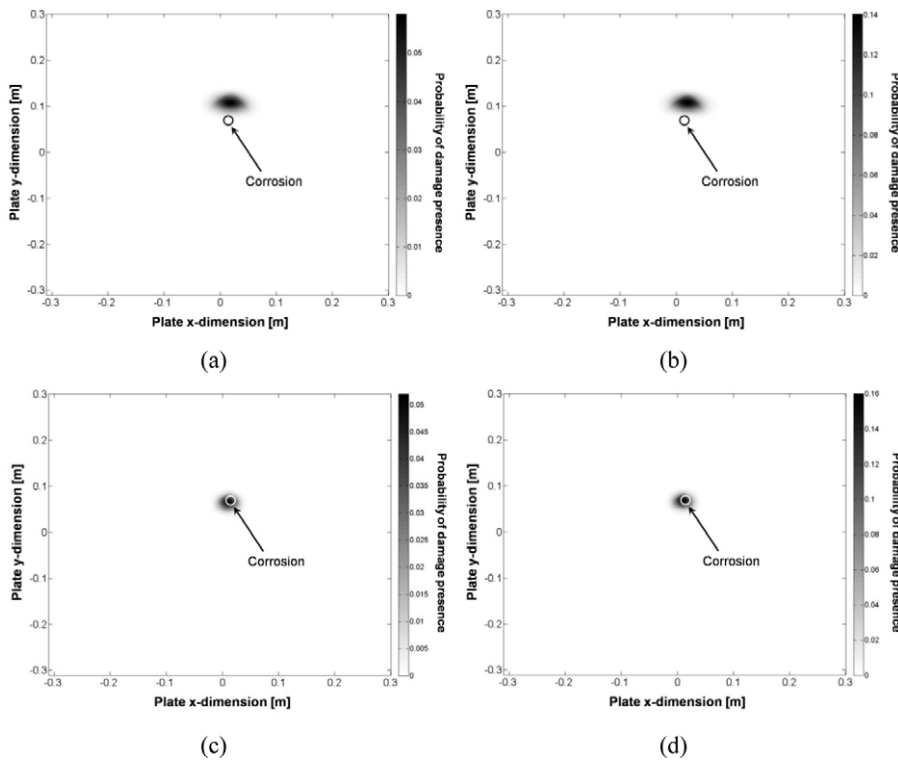


**Figure 20.** Identification results of corrosion damage in the aluminium plate coupled with fluid layer of different thicknesses: (a) without rectification when the fluid layer is 4 mm in thickness; (b) without rectification when the fluid layer is 7 mm in thickness; (c) with compensation for the coupling effect when the fluid layer is 4 mm in thickness, and (d) with compensation for the coupling effect when the fluid layer is 7 mm in thickness (white or black circle: actual corrosion).

11

through-thickness hole and chemical corrosion in submerged aluminium plates was identified precisely with the assistance of a probability-based diagnostic imaging approach. The results have demonstrated the necessity of rectification and compensation for medium coupling in practice when applying Lamb-wave-based damage identification to structures with coupled media.

## Acknowledgments

## References

[1] Jones D 1996 *Principles and Prevention of Corrosion* 2nd edn (Upper Saddle River, NJ: Prentice-Hall)

[2] Jenot F, Ouaftouh M, Duquennoy M and Ourak M 2001 Corrosion thickness gauging in plates using Lamb wave group velocity measurements *Meas. Sci. Technol.* **12** 1287–93

[3] Bayliss M, Short D and Bax M 1988 *Underwater Inspection* (London: E & F N Spon)

[4] Nordbø H 1986 NDE-overview and legal requirements *Submersible Technology* (London: Graham & Trotman Ltd) pp 183–7

[5] Upda L, Mandayam S, Upda S, Sun Y and Lord W 1996 Development in gas pipeline inspection technology *Mater. Eval.* **54** 467–71

[6] Mandal K, Dufour D, Krause T W and Atherton D L 1997 Investigations of magnetic flux leakage and magnetic Barkhausen noise signals from pipeline steel *J. Phys. D: Appl. Phys.* **30** 962–73

[7] Na W B and Kundu T 2002 Underwater pipeline inspection using guided waves *J. Pressure Vessel Technol.* **124** 196–200

[8] Staszewski W J, Boller C and Tomlinson G R 2004 *Health Monitoring of Aerospace Structures: Smart Sensor Technologies and Signal Processing* (New York: Wiley)

[9] Badcock R A and Birt E A 2000 The use of 0–3 piezocomposite embedded Lamb wave sensors for detection of damage in advanced fibre composites *Smart Mater. Struct.* **9** 291–7

[10] Guo N and Cawley P 1993 The interaction of Lamb waves with delaminations in composite laminates *J. Acoust. Soc. Am.* **94** 2240–6

[11] Park H W, Sohn H, Law K H and Farrar C R 2007 Time reversal active sensing for health monitoring of a composite plate *J. Sound Vib.* **302** 50–66

[12] Lemistre M and Balageas D 2001 Structural health monitoring system based on diffracted Lamb wave analysis by multiresolution processing *Smart Mater. Struct.* **10** 504–11

[13] Mijarez R, Gaydecki P and Burdekin M 2007 Flood member detection for real-time structural health monitoring of sub-sea structures of offshore steel oilrigs *Smart Mater. Struct.* **16** 1857–69

[14] Maze G, Cheeke J D N, Li X and Wang Z 2001 Coupled guided acoustic modes in water-filled thin-walled tubes *J. Acoust. Soc. Am.* **110** 2295–300

[15] Cheeke J D N, Shannon K and Wang Z 1999 Loading effects on $A_0$ Lamb-like waves in full and partially filled thin-walled tubes *Sensors Actuators* B **59** 180–3

[16] Rose J L 1999 *Ultrasonic Waves in Solid Media* (Cambridge: Cambridge University Press)

[17] Monkhouse R S C, Wilcox P D and Cawley P 1997 Flexible interdigital PVDF transducers for the generation of Lamb waves in structures *Ultrasonics* **35** 489–98

[18] Moilanen P, Nicholson P H F, Kilappa V, Cheng S and Timonen J 2006 Measuring guided waves in long bones: modeling and experiments in free and immersed plates *Ultrasound Med. Biol.* **32** 709–19

[19] Diamanti K, Soutis C and Hodgkinson J M 2005 Lamb waves for the non-destructive inspection of monolithic and sandwich composite beams *Composites* A **36** 189–95

[20] Grondel S, Paget C, Delebarre C, Assaad J and Levin K 2002 Design of optimal configuration for generating $A_0$ Lamb mode in a composite plate using piezoceramic transducers *J. Acoust. Soc. Am.* **112** 84–90

[21] Kessler S S, Spearing S M and Soutis C 2002 Damage detection in composite materials using Lamb wave methods *Smart Mater. Struct.* **11** 269–78

[22] Giurgiutiu V and Cuc A 2005 Embedded non-destructive evaluation for structural health monitoring, damage detection, and failure prevention *Shock Vib. Dig.* **37** 83–105

[23] Wang L and Yuan F G 2007 Group velocity and characteristic wave curves of Lamb waves in composites: modeling and experiments *Compos. Sci. Technol.* **67** 1370–84

[24] Ghosh T, Kundu T and Karpur P 1998 Efficient use of Lamb modes for detecting defects in large plates *Ultrasonics* **36** 791–801

[25] Giurgiutiu V 2005 Tuned Lamb wave excitation and detection with piezoelectric wafer active sensors for structural health monitoring *J. Intell. Mater. Syst. Struct.* **16** 291–305

[26] Qing X P, Chan H-L, Beard S J and Kumar A 2006 An active diagnostic system for structural health monitoring of rocket engines *J. Intell. Mater. Syst. Struct.* **17** 619–28

[27] Su Z and Ye L 2005 Lamb wave propagation-based damage identification for quasi-isotropic CF/EP composite laminates using artificial neural algorithm, part I: methodology and database development *J. Intell. Mater. Syst. Struct.* **16** 97–111

[28] Su Z, Wang X, Cheng L, Yu L and Chen Z 2009 On selection of data fusion schemes for structural damage evaluation *Struct. Health Monit.: Int. J.* **8** 223–41

[29] Konstantinidis G, Drinkwater B W and Wilcox P D 2006 The temperature stability of guided wave structural health monitoring systems *Smart Mater. Struct.* **15** 967–76

[30] Michaels J E 2008 Detection, localization and characterization of damage in plates with an *in situ* array of spatially distributed ultrasonic sensors *Smart Mater. Struct.* **17** 035035

[31] Chen H G, Yan Y J, Chen W H, Jiang J S, Yu L and Wu Z Y 2007 Early damage detection in composite wingbox structures using Hilbert–Huang transform and genetic algorithm *Struct. Health Monit.: Int. J.* **6** 281–97

[32] Zhao X, Gao H, Zhang G, Ayhan B, Yan F, Kwan C and Rose J L 2007 Active health monitoring of an aircraft wing with embedded piezoelectric sensor/actuator network: I. Defect detection, localization and growth monitoring *Smart Mater. Struct.* **16** 1208–17

[33] Ihn J-B and Chang F-K 2008 Pitch-catch active sensing methods in structural health monitoring for aircraft structures *Struct. Health Monit.: Int. J.* **7** 5–19

[34] Wang C H, Rose J T and Chang F-K 2004 A synthetic time-reversal imaging method for structural health monitoring *Smart Mater. Struct.* **13** 415–23

[35] Ang A H S and Tang W 1975 *Probability Concepts in Engineering Planning and Design* vol 1 *Basic Principles* (New York: Wiley)